DOI: 10.1002/cphc.201000812

Innovative Measurement Techniques in Surface Science

Hans-Joachim Freund,* Niklas Nilius, Thomas Risse, Swetlana Schauermann, and Thomas Schmidt[a]

We describe four new experimental techniques advanced during the last decade in the authors' laboratory. The techniques include photon scanning tunneling microscopy; aberration-corrected low-energy electron microscopy in combination with photoelectron emission microscopy, microcalorimetry, and electron-spin resonance spectroscopy. It is demonstrated how those techniques may be applied to solve fundamental problems in surface science with growing demands to tackle complex nanoscopic systems, and, in particular in catalysis science, which, without the availability of those techniques, would be difficult if not impossible to address.

1. Introduction

Science and knowledge has always progressed in major steps when new measurement techniques became available. This is particularly true for surface science. In fact, the entire field started to develop in the second half of the sixties due to the introduction of ultrahigh vacuum technology, which in turn enabled the development of new experimental techniques.[1,2] Those allowed the scientific community to come to an atomistic understanding of solid surfaces. Typical examples of how much may be gained through method development are the various scanning probe techniques.[3] Their ability to access real space information on surfaces beyond classical electron microscopy has changed our perception about surfaces, because seeing is believing. Without them, the current nanoscience initiatives,[4] encompassing chemistry, physics and biology, would have been impossible. While this is easily agreed upon once the technique has demonstrated its potential in the scientific community, it is often forgotten that the pathway to its development has been nothing but smooth. Not only because it might have been difficult to develop the experiment or due to the lack of craftsmanship, an important stumbling block often has been the lack of support. In many cases progress was only possible because researchers were deviating from the canonical path. It is simply impossible to perform risky research projects, and instrument development is such a risky field, within two- to three-year project schedules. One needs long-term support, and this article is, in addition to reporting progress in developing experimental techniques in the authors' laboratory, a plea for such kind of support. Without having the institutional support of the organization (www.mpg.de) supporting the authors, and the independence from administrative restrictions, it would have been impossible to bring the development described below to completion.

Herein, we briefly touch upon the scientific questions we are trying to answer in order to provide a way for the reader to understand how the necessity for building equipment developed. Surface science has greatly contributed to a number of fields of technological importance, such as semiconductor device physics, catalysis science, storage media, IT applications, and even certain areas of organic, inorganic, and biological chemistry.[2] One scheme that runs through many of those is the investigation of nanostructured materials. Our focus has been catalysis with the goal to understand disperse metal and oxide catalysts at the atomic scale. Appropriate samples in this field are considerably more complex than for example, metal single crystals. In turn, a combination of techniques is generally required to achieve a complete picture and avoid overinterpreting individual results. This necessity to characterize the numerous properties of interest is the main driving force for instrument development. This also implies a certain compatibility of the techniques in the sense that the same samples may be studied with each technique.

We already referred to scanning probe microscopy. A disadvantage of those techniques is their inherent chemical insensitivity.[5] This disadvantage also applied to electron microscopy and was only turned into an advantage when combining it with local spectroscopy, in this case electron energy loss spectroscopy. In the case of scanning probe techniques, the disadvantage may be overcome by detecting the bias dependence of electron transport into the sample (scanning tunneling spectroscopy), or the fluorescence signal generated by locally exciting the surface with electrons from the tip. For the latter case a photon-scanning tunneling microscope, as proposed by Gimzewski et al[6] has been developed to study the optical characteristics of metal particles, and, recently, defect structures in oxide surfaces. Parallel to this, a new aberration-corrected instrument for low-energy electron microscopy (LEEM), and photoelectron emission microscopy (PEEM), as proposed by Rose et al. is under development.[7,8] This is a long-term development, and was, in fact, held up by the way it was funded in the beginning. This instrument will allow us to address individ-

[a] *Prof. H.-J. Freund, Dr. N. Nilius, Dr. T. Risse, Dr. S. Schauermann, Dr. T. Schmidt*
Fritz-Haber Institut der Max-Planck Gesellschaft
Faradayweg 4-6, 14195 Berlin (Germany)
Fax: (+49) 30 84134101
E-mail: freund@fhi-berlin.mpg.de

ual nanoparticles supported on surfaces and take photoelectron and near-edge X-ray absorption spectra of such individual particles and adsorbates on them. Both methods will provide unprecedented input to our understanding of the chemistry of supported catalysts.

In addition to providing access to information on individual nano-objects, it is also important to be able to determine key quantities of particle ensembles. Thermodynamic quantities such as adsorption energies are of particular interest as they provide benchmarks for comparison with bulk systems and also for any theoretical development. Since particle systems are not stable under thermal treatment, classical thermal desorption techniques (TDS), typically applied at surface systems, cannot be used in this case. Other limitations arises from the fact that TDS provides reliable results only for systems with fully reversible adsorption, which means that most catalytically relevant processes involving dissociation, reaction with co-adsorbates, clustering or diffusion into the bulk cannot be correctly probed by nonisothermal methods. Microcalorimetry as developed by King et al.[9] and improved by Campbell et al.[10] is a solution. We have built a microcalorimeter with sufficient sensitivity to be able to measure temperature-dependent heats of adsorption on nanoparticle ensembles with aggregates sizes ranging down to about hundred atoms.[11,12]

There are already many spectroscopic techniques available to investigate particle ensembles, but techniques based on magnetic resonance are scarce in surface science. This is mainly caused by the low sensitivity of nuclear magnetic resonance, so popular in many other fields of material science. Because of this low sensitivity, recording NMR signals from single-crystal surfaces is not possible in a conventional manner. As shown by Fick et al.,[13] highly polarized nuclear spin populations are required to overcome this problem, which up to now has considerably restricted the applicability of the method. On the other hand, electron spin resonance provides the necessary sensitivity for this type of research, as demonstrated by Baberschke et al.[14] If such an experiment would be feasible, interesting information that is out of reach for other techniques could be obtained. In addition, electron spin resonance represents a photon-in–photon-out technique, and is as such applicable not only in ultrahigh vacuum, but also in an ambient environment.

In the following chapters, developments made in the authors' laboratory on the techniques described above are presented and exemplified on the basis of recent results.

2. Fluorescence Spectroscopy with the STM

Classical wave optics sets a natural limit to the spatial resolution that is achievable by far-field optical techniques. However, electron injection into the sample is used in fluorescence spectroscopy with an STM[15] to overcome the limits of optical microscopy. As the diameter of the exciting electron beam from the STM tip is hereby not larger than 1 nm^2, optical properties can be probed with unmatched spatial resolution even though detected in the far field.

Optical spectroscopy with an STM is feasible only because of the distinct nature of the tip–sample cavity to act as an electromagnetic resonator.[16] The hereby tip-induced plasmons (TIP) are driven by high-frequency fluctuations of the tunnel current, while the required energy is provided by inelastic electron transport through the STM junction. The field enhancement that is associated with the TIPs may easily reach a factor of thousand. Due to an antenna-like effect, such strong near-fields dramatically increase the spontaneous emission rate of a dipole source placed in the STM junction. Only this enhancement effect renders light emission from individual centers detectable in the far field.

Despite of the field amplification, the detection of photons from an STM contact remains challenging. In our setup, a beetle-type STM head was surrounded by a parabolic mirror of 45 mm diameter and 10 mm focal length, which collects light from about 30% of the total solid angle of 4π (Figure 1a).[17] A second off-axis parabolic mirror is placed outside the vacuum chamber to refocus the light onto the two available detectors. The first one is a liquid-nitrogen- (LN_2) cooled CCD chip coupled to a grating spectrograph and used to analyze the wavelength distribution of the emitted light between 200 and 1200 nm. The second one is a photomultiplier tube that

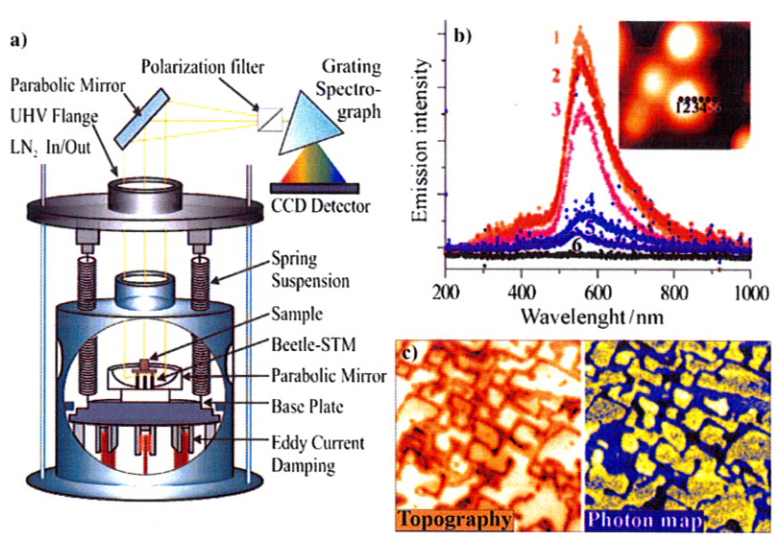

Figure 1. a) Experimental setup to detect photons from an STM junction. b) Emission spectra of a single Au particle on TiO_2(110) [$U_S = 5$ V, $I = 2$ nA]. The spectral positions on the particle are depicted in the inset (30×30 nm^2). c) Topographic image and photon map of a 10 ML thick MgO film on Mo(001) [100×100 nm^2]. At the selected excitation bias of 5.1 V, surface regions with low work function appear with bright contrast.

probes the integral optical response and is employed to acquire spatial maps of the emission yield. Those photon maps are measured simultaneously with a topographic image and enable the direct identification of optically active sites at the surface. A Glenn–Thomson prism placed in front of either the two detectors allows us to probe the polarization of the photons in addition. Alternative setups to detect the radiation from an STM junction have been realized in other groups.[18,19]

We have advanced the technique of STM-based optical spectroscopy in two directions, by performing experiments on single metal nanoparticles and oxide materials. Both systems are characterized by highly inhomogeneous optical properties across their surface. The emission response of nanoparticles depends sensitively on their geometry as well as on interactions with adjacent particles and the substrate.[20] The capability of the technique in terms of spatial resolution is demonstrated in Figure 1b, which displays a set of emission spectra taken across a single Au particle on a TiO_2(110) surface. Spectra of the particle centre reveal a strong emission line at 550 nm that is assigned to an out-of-plane plasmon excitation.[20] The peak gradually loses intensity and finally disappears when moving the tip over the particle edge onto the oxide surface. From the evolution of the emission signal with tip position, the lateral resolution of the method is estimated to be of the order of 1 nm. The technique has been extensively exploited to study the emission properties of nanoparticles as a function of their size, shape, chemical composition and interparticle coupling.[21,22] For example, chemically different aggregates (Mg, Ca and Au) as well as alloys,[23] could be identified on an MgO support via their specific optical response. Furthermore, a distinct blue-shift of the emission peak has been observed for Ag particles of decreasing size, reflecting the vanishing influence of d electrons on the s-like plasmons in ultrasmall aggregates.[21] Finally, mutual coupling between plasmonic and excitonic excitations was studied for different particle-oxide systems, providing insight into an elementary energy-transfer process occurring in photochemical reactions.[24]

A second focus of our work lies in the optical characterization of pristine oxide materials. Their optical properties are governed by the excitation and radiative decay of electron–hole pairs, being closely associated with the defect structure and therefore spatially inhomogeneous as well.[25] Light emission due to exciton recombination has been detected on MgO(001) films upon injection of energetic electrons ($E_{kin} >$ 25 eV).[26] The two emission bands at 3.1 and 4.4 eV were hereby assigned to excitons trapped at low-coordinated sites in the MgO surface. With decreasing electron energy, electron–hole-pair formation becomes impossible due to the large oxide band gap of ~8 eV. However, a second optical channel opens between 5.5–8.0 V excitations bias, when electrons are injected into image-potential states at the oxide surface and decay radiatively to the MgO conduction band onset.[27] The threshold bias for exciting this particular emission depends strongly on the sample work function and maps of the emission intensity therefore provide information on the spatial distribution of the work function across the oxide film. A corresponding photon map is presented in Figure 1c. In the left panel, the morphology of the MgO film is shown, whereby defect-free oxide terraces appear in bright colour and a network of separating dislocation lines in dark colour. The right panel displays the corresponding photon-intensity distribution, measured simultaneously in the same surface region. At the selected bias of 5.1 V, the oxide terraces with their low work function are optically active, as only there electrons have enough energy to reach the image potential states. The line defects, on the other hand, have a considerably higher work function and the emission channel opens only above 6.0 V sample bias. This increase in the local work function is attributed to the ability of such defects to trap electrons, which in turn induce a large negative surface dipole.[27] Fluorescence spectroscopy with the STM is among the few methods that are able to explore the chemically important phenomenon of electron trapping at an atomic scale.

One direction in which fluorescence spectroscopy with an STM will develop in the future is to link the unique spatial resolution of STM to the high temporal resolution of a pump-probe optical experiment.

3. A Project to Build a *Spectro*microscope with *A*berration Correction for many *R*elevant *T*echniques (SMART)

Within a collaboration including groups from universities Würzburg, Erlangen, Clausthal, the Zeiss company, BESSY, and the Fritz Haber Institute of the Max Planck Society, a new type of spectromicroscope that combines a "normal" LEEM/PEEM instrument with aberration corrections (both, chromatic and spherical) and energy resolution using an imaging energy analyzer has been designed and built. This instrument, called SMART[28,29] and installed at BESSY II, is aimed at the spectroscopic and structural characterization of individual nanoparticles supported on oxide films. Theory predicts a lateral resolution of 0.5 nm at an energy resolution of less than 100 meV, whereby the transmission is increased nearly a hundred times compared to conventional LEEM/PEEM instruments due to the large acceptance angle of SMART. In fact, this instrument delivered a lateral resolution of 2.6 nm and an energy resolution of 180 meV together with an increase in transmission of about one order of magnitude (compared to standard PEEM instruments). This was possible only by fulfilling three major conditions: 1) improvement of the electron optical design by aberration correction, 2) highly stable sources for the magnetic and electrostatic fields and precise mechanical alignment of the optical elements, and 3) protection against external perturbations by electromagnetic shielding and vibration damping. Especially with respect to aberration correction, groundbreaking work has been done within the SMART project: the tetrode electron mirror together with a highly symmetric magnetic beam splitter as suggested by Rose and Preikszas[7,8] has been the first successfully working aberration corrector that compensates simultaneously for spherical and chromatic aberration of the electron lens system. The second innovation is the first UHV version of the magnetic OMEGA filter which represents a second-order aberration-corrected imaging electron energy an-

alyzer. With a spatial resolution smaller than one thousandth of the field of view the imaging quality is the best ever achieved for an energy filter, and is capable of delivering the highest energy resolution.

Besides these unique electron optical properties, the SMART excels as a versatile instrument for comprehensive surface characterization .[30] Utilizing different sources [linearly or circularly polarized X-rays, ultraviolet (UV) light, electron gun, etc.] the SMART offers a variety of contrast mechanisms[31] by imaging photoemitted and reflected electrons. Thus it enables spatially resolved investigations of morphology, chemical distribution, electronic state, molecular orientation, magnetization, work function, structural properties, atomic steps, and so forth. As LEEM/PEEM in general, the SMART is a directly (i.e. nonscanning) imaging instrument allowing for real-time observation of surface processes at video rate or even faster. Due to sample heating and LN_2 cooling the surface can be studied in situ within a temperature range of 130 K and 2000 K, enabling the investigation of temperature-dependent processes such as phase transitions, desorption, chemical reaction or crystal growth. By dosing gases into the specimen chamber up to a pressure of 10^{-5} mbar, surface chemical reactions have been observed directly with this kind of instrument.[32,33]

In contrast to the widely used TEM and SEM (transmission and scanning electron microscopes) the kinetic electron energy at the sample is low for a LEEM/PEEM, typically in the range of 1 to 500 eV. Beside the reduced risk of beam damage, this has the advantage of a small probing depth of the order of a nanometer.

If soft X-rays with a typical photon energy range of 100 eV to 1000 eV are used to illuminate the sample, a whole energy spectrum of electrons is emitted. The energetic position of the spectral lines may be assigned to a specific element, and, moreover, energetic shifts of the lines are related to the chemical state of the related atoms. With the energy filter a specific ionization and therefore a corresponding element can be selected. Only the electrons belonging to this line are used for imaging. As a consequence, just these surface areas appear bright in the microscopic image, which contain high concentrations of the selected elements. By scanning the energy window over the whole XPS, the chemical composition is mapped within spatial resolution of the instrument.

Additionally to the spectroscopic contrast, the SMART offers structural contrast by illuminating the sample with electrons produced by a highly brilliant electron gun and imaging the elastically reflected electrons (LEEM). For crystalline samples the wave nature of electrons is used for imaging. The periodic arrangement of atoms in the crystal and at the surface produces a specific electron diffraction pattern (LEED) from which one deduces the structures of the crystal and the adsorbate. In LEEM the diffraction contrast visualizes different crystalline structures, surface superstructures, facets and single atomic steps. By aberration correction the SMART reaches a lateral resolution of 2.6 nm in LEEM, which enables the direct observation of tiny structures such as the herringbone superstructure of the Au(111)-$(22\times\sqrt{3})$ surface, which would not have been possible without aberration correction, due to the resolution

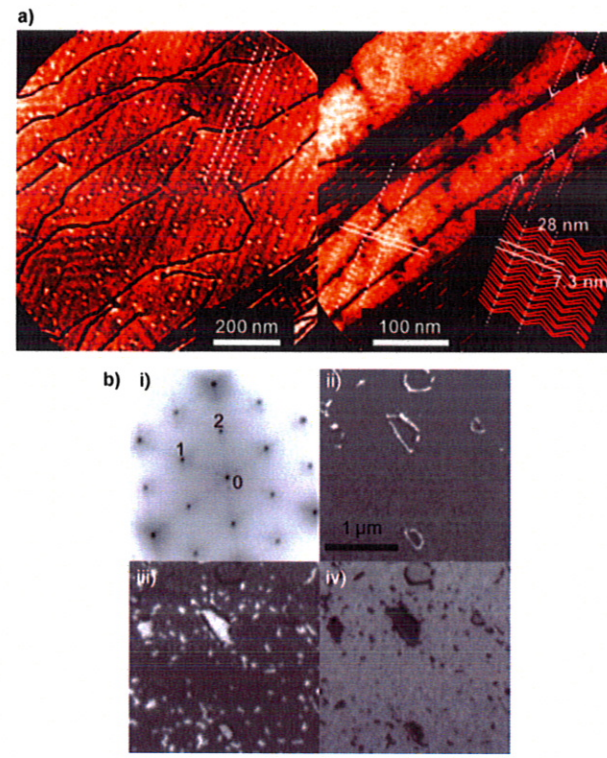

Figure 2. a) LEEM image of the Au(111) herringbone structure for two different focusing conditions, showing the two different periodicities (see model in the inset). b) Fe_3O_4 film on Pt(111) surface with structural and morphological defects. The LEED pattern (i) shows a superposition of the (2×2) superstructure of the Fe_3O_4 film and additional spots surrounding the central (00) spot resulting from a Moiré pattern of a FeO film. The LEEM images use different LEED spots: ii) Bright-field image using the central (00) spot, labeled with '0' in (i). iii) and iv) Dark-field images using the superstructure spot labeled with '1' and '2', respectively.

limit of about 4 nm. Figure 2a shows large terraces on a Au(111) surface with atomic steps (dark lines) and contamination with carbon clusters (white dots). Additionally a striped pattern with weaker contrast is visible (indicated by dotted lines) with two directions: rotated by 120° except for the lower left where the contrast lines run horizontal. The observed periodicity of 28 nm $\pm$0.5 nm corresponds to the distance of the elbows in the herringbone reconstruction[34] (see model in right inset) found on large terraces.[35] The herringbone structure arises from a reconstruction of the Au(111) surface which contains a tighter arrangement of Au atoms than the hexagonal close packing and a large unit cell. It gives rise to reconstruction lines arranged in a herringbone structure with straight sections and elbows. This superstructure consists of an alternating arrangement of fcc and hcp surface areas. The difference in the local crystalline structure is the reason for the diffraction contrast, so that the different types of elbows appear as dark and bright lines. At higher magnification and slightly changed diffraction conditions even the higher frequency of 7.3 nm becomes visible (Figure 2b),[36] which is only possible if the lateral resolution is considerably better than half the period length (< 3.7 nm). Understanding the development of oxide film growth morphology is a necessary prerequisite to investigate metal nanoparticles supported on those oxides be-

cause their stability will be strongly influenced by surface termination and defect structure of the oxide. Using the LEEM options of the instrument allow us to study, for example, the growth of a magnetite film on a Pt(111) single-crystal substrate, using a recipe developed by our group. The LEED pattern in Figure 2b i shows the coexistence of a hexagonal structure, expected for the nominal 2.6 nm thick Fe_3O_4 film in the (111) orientation, and of a Moiré pattern which leads to additional spots surrounding the central (00) spot, related to the presence of an FeO film on Pt(111).[37] The bright-field image (Figure 2b ii), obtained by using the zero-order diffraction spot together with the spots of the Moiré pattern, shows bright ring-like white patches, which cover about 2% of the entire surface. These patches appear dark in the dark-field images (Figure 2b iii,iv) when taken with the first-order diffraction spots of the magnetite. Therefore these areas are regions where a FeO bilayer emerges and are not covered by the magnetite thin film. Only thicker oxide films are sufficiently stabilized to allow the application of higher oxidation temperatures, which is important to perform the studies envisioned. Eventually this will allow us, in combination with the PEEM options of the instrument, to look at structure–reactivity correlations on individual nanoparticles on oxides, which in turn will be a major step forward in understanding heterogeneous chemistry, which is so important within heterogeneous catalysis.

4. Single-Crystal Adsorption Calorimetry

In order to link our detailed knowledge on particles structures to the energetics of gas–surface interactions, a new microcalorimeter has been built and integrated into an ultrahigh vacuum apparatus (for more details see ref. [12]). This setup allows for in situ preparation of well-defined supported model catalysts on ultrathin (1–10 μm) metal single crystals and measurement of adsorption and reaction heats in a broad temperature region ranging from 100 to 300 K. The method of single-crystal adsorption calorimetry (SCAC) relies on the measurement of a temperature rise upon adsorption of molecules on the ultrathin single crystals, which is recorded via a pyroelectric detector and an independent laser-based energy calibration. Briefly, in a microcalorimetric experiment, a pulse of gas from a chopped molecular beam impinges on a crystal surface and a fraction of the molecules striking the surface adsorbs, causing a transient heat input and a temperature rise. This small change in temperature (a few mK) is measured by a pyroelectric heat detector, consisting of a β-polyvinylidine fluoride (β-PVDF) ribbon coated with a metal on both sides, which produces a voltage signal upon heat transfer. The absolute signal calibration is performed by applying pulses of laser light of known energy, which pass through the molecular beam and are chopped in a way identical to the molecular flux. Simultaneously, the absolute number of molecules adsorbed in a single beam pulse is determined by a sticking coefficient measurement via the King–Wells method.[38]

Figure 3a shows the main components of the experimental arrangement of the adsorption/reaction chamber, which includes a high-flux effusive molecular beam (1) (up to

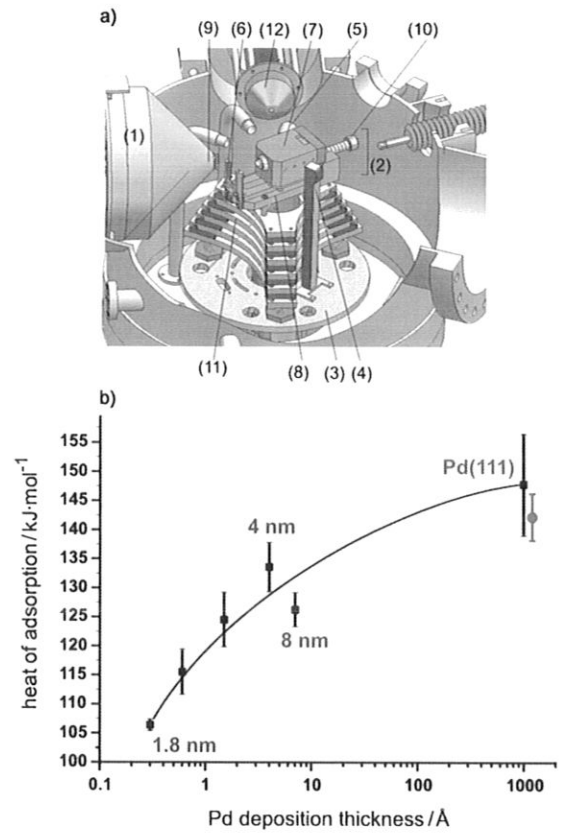

Figure 3. a) Overview of the main components in the adsorption/reaction chamber. The labeled components are: 1) molecular beam source, 2) microcalorimeter, 3) rotatable platform, 4) in situ photodiode, 5) beam monitor, 6) sample holder mounting, 7) movable detector head of the microcalorimeter, 8) Cu platform carrying the sample holder mounting and the detector, 9) outer molecular beam aperture, 10) translation screw, 11) vibration damping stack, 12) quadrupole mass spectrometer. b) Initial heat of adsorption of CO as a function of Pd coverage measured on the Fe_3O_4/Pt(111) samples with the nominal deposition thickness of 0.3, 0.6, 1.5, 4 and 7 Å and on the Pd(111) single-crystal surface. Each point in this curve is an average of 4 to 6 independent measurements on freshly prepared model systems. Error bars: the standard error of the mean. The grey circle corresponds to the value of the CO adsorption heat on Pd (111) reported by Ertl et al.[39]

2×10^{15} molecules $cm^{-2}s^{-1}$) with an integrated chopper and the tools for laser-calibration purposes (for details see ref. [12]) as well as the microcalorimeter (2). The absolute accuracy of the heat values critically depend on the absolute intensity of the laser light, the reflectivity of the sample and the absolute flux of molecules impinging on the sample surface. To accurately determine these parameters, three corresponding in situ detectors were additionally integrated into the vacuum system. A differentially pumped rotatable platform (3) mounted in the center of the adsorption/reaction chamber carries the microcalorimeter (2) and two additional detectors: a UHV-compatible photodiode (4) for in situ determination of the absolute laser intensity and a beam monitor (5) for measurement of the absolute molecular beam fluxes. The third detector for in situ determination of the reflectivity of the sample is set up in a separate preparation chamber (not shown here).

The entire microcalorimeter can be cooled down to liquid nitrogen temperature or with a cooled gas to cryogenic tem-

peratures. For this, the microcalorimeter is connected to a thermal reservoir made of Cu, whose large mass (about 2 kg) provides sufficient temperature stability within hundreds of minutes. For the measurement of the molecular beam flux and the laser intensity calibration the platform (3) can be rotated to bring the corresponding detectors—the beam monitor (5) and the photodiode (4)—in front of the molecular beam at a distance of 4 mm, which is exactly the same as the position of the sample during the microcalorimetric measurement. This allows one to minimize the systematic errors due to misalignments of different types of detectors.

For the present setup, detector sensitivities of 8–40 $V\,\mu J^{-1}\,cm^{-2}$ was achieved with a noise-limited resolution of about 120 $nJ\,cm^{-2}$. The detection limit of the calorimeter for CO adsorption on clean Pt(111) was estimated to be 1.5×10^{12} molecules $cm^{-2}\,s^{-1}$, corresponding to a coverage of less than 0.1% of a monolayer, with respect to the number of surface atoms of Pt(111). We obtained the absolute accuracy in energy to within a few percent.

To address the correlation between the structure of the nanoparticles and the energetics of the gas–surface interactions, we studied CO adsorption on Pd nanoclusters as a function particle size. Figure 4b shows the initial heats of CO adsorption on the Pd particles supported on a Fe_3O_4/Pt(111) oxide film for five different nominal Pd deposition thicknesses (0.3, 0.6, 1.5, 4 and 7 Å) and on Pd(111), corresponding to particle sizes between ~120 and ~4900 Pd atoms per particle (corresponding to particle diameters from 1.8 to 8 nm).

The dependence of initial CO adsorption heats on the particle size shows a pronounced trend. The initial heat of adsorption decreases with the nominal Pd deposition thickness, that is, with decreasing particle size, from 126 ± 7 $kJ\,mol^{-1}$ on 8 nm-sized Pd particles to 106 ± 2 $kJ\,mol^{-1}$ on the smallest 1.8 nm clusters. All investigated particles showed smaller initial adsorption enthalpy as compared to the single-crystal surface (149 $kJ\,mol^{-1}$). It may be of interest to compare the calorimetrically measured adsorption enthalpies with corresponding thermal desorption data. However, such a comparison is difficult, as the ensemble of nanoparticles changes during temperature ramp, which is particularly significant for the smallest particles. Therefore, calorimetry is the only way forward to access this information reliably.

There are two counteracting trends that can potentially account for the changes in the adsorption energy with the decreasing particles' dimension. First, with decreasing cluster size a larger fraction of the low-coordinated sites is created, which exhibit higher adsorption energies as compared to the regular (111) facets[39,40] and consequently would lead to increasing initial adsorption energies. Since an opposite trend is observed experimentally, we conclude that this effect cannot play a major role in determining how CO adsorption energies vary with particle size for Pd. Second, the initial CO adsorption heat may decrease with decreasing particles size as a result of two effects: 1) weakening of the chemisorptive interaction and 2) reduction of the Van der Waals attraction. Previously, it has been demonstrated experimentally[41] and confirmed theoretically[42] that the interatomic bond length in small metal particles decreases with decreasing particle size. This lattice contraction in small metal clusters was theoretically shown to result in a reduction of adsorbate binding energy[43] corresponding to the principle of bond-order conservation.[44] A second reason for the decrease of adsorption heat of a gas-phase molecule on small metal clusters is a weakening of the dispersion force (Van der Waals interaction) that is induced by dynamic response of bulk electrons of the metal to charge density fluctuations in an adsorbed molecule. Since smaller clusters contain fewer electrons available for dynamic response, the gradual decrease of the initial adsorption heat with decreasing cluster size may be understood. Similar behavior has been previously observed in, however, inconclusive TPD studies for methane on Pd[45] and NO on Ag nanoclusters[46] and was

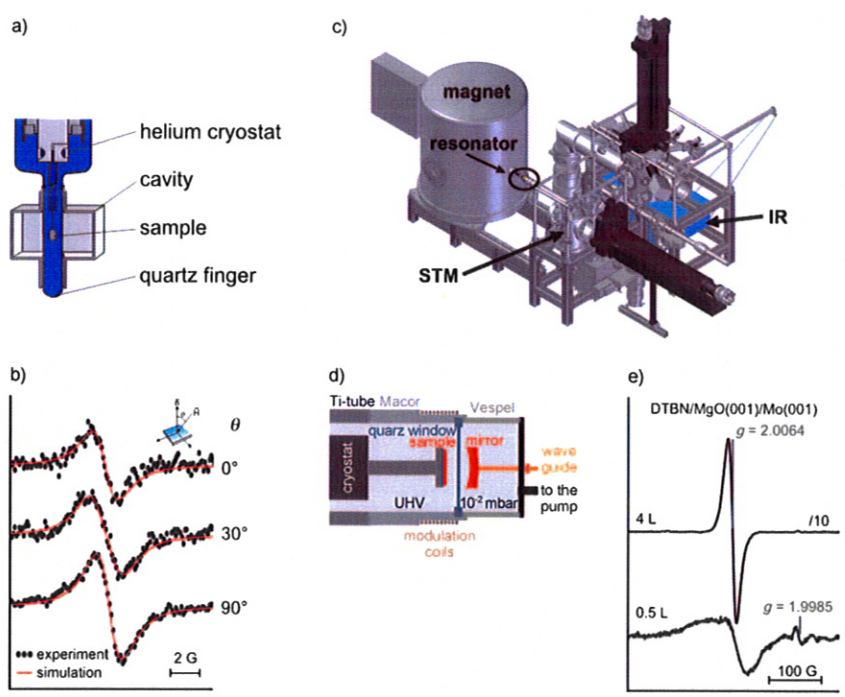

Figure 4. a) UHV-compatible ESR setup used for X-band (10 GHz) measurements. b) ESR spectra of F^+ centers taken at 300 K on an electron-irradiated 20 ML thick MgO(001)/Mo(001).[52] c) Technical drawing of the UHV-compatible W-band spectrometer showing the preparation chamber with the IR spectrometer in the back and the analysis chamber with the ESR and STM facilities in the front. d) Fabry-Perot resonator setup (top) and the coupling antenna (bottom). e) W-band ESR spectra of DTBN on a 20 ML MgO(001)/Mo(001) film.

also attributed to the reduced polarizability of the small metal nanoparticles.

5. Development of EPR Spectroscopy to Study Single-Crystal Surfaces

ESR spectroscopy was used to address surface problems early on (e.g. refs. [47–49]), but measurements on single-crystal surfaces under ultrahigh vacuum conditions are scarce. What is the reason for this? One has to keep in mind that the technique is rather restricted in terms of applicable systems—it requires either paramagnetic or ferromagnetic samples—and, moreover, is not inherently surface sensitive. On the other hand, ESR spectroscopy can determine the characteristic magnetic parameters characterizing the system with high precision. These parameters (e.g. the g- and hyperfine tensors) encode the geometric as well as electronic properties of the system and it does so for systems that are often difficult to access with conventional surface-science techniques. On a single-crystal surface one can not only determine the values of the magnetic parameters but also their orientation with respect to the surface, which can be translated into geometric information. Despite the limitation to paramagnetic or ferromagnetic samples, there is a variety of interesting classes of species that can be investigated by ESR spectroscopy. These range from paramagnetic transition metal atoms and ions, structural defects such as anion vacancies on oxide surfaces, paramagnetic adsorbates all the way to reaction intermediates and the group has studied examples for each of these (e.g. refs. [50–57]). The lack of surface sensitivity can be addressed in straightforward fashion, for example by the physisorption of molecular oxygen at low temperature which suppresses the ESR signal from surface species due to its relaxation properties.

All EPR experiments on single-crystal surfaces performed under ultrahigh vacuum conditions so far were continuous-wave (cw) experiments at the X-band (around 10 GHz). The design used in our group goes back to a setup of the Baberschke group developed in the late 1980s.[14,53,58] The lower part of the chamber consists of a glass-to-metal seal and ends in a quartz finger with an outer diameter of about 10 mm, as shown in Figure 4a, and is inserted into a conventional ESR cavity (TE_{102} in our case). With these dimensions, the single crystals can have a surface area of about 1 cm^2. It is decisive to align the crystal appropriately in the cavity. This limits the reduction of its loaded quality factor to the minimum. Even though the general setup remained the same, a variety of changes in the sample setup has allowed an improvement of the sensitivity and especially the long-term stability of the system, such that the detection limit is currently around 5×10^{11} spins cm^{-2}. The exact figure, however, depends upon the nature of the species (line width, spectral width, relaxation properties, etc.). This sensitivity allows detecting minority sites on surfaces. To this end, defects and particularly point defects are suitable species which affect the chemical properties of oxide surfaces considerably. As shown in Figure 4b ESR spectroscopy is capable to detect paramagnetic F^+ centers on single-crystalline MgO(001) surfaces whose concentration were estimated to be 5×10^{-11} spins cm^{-2}.[52] The signal of the F^+ centers shows an angular dependence which is governed by the anisotropy of the Zeeman interaction (g-tensor). From these measurements the orientation of the tensor can be determined and the majority of the species were inferred to be located on edges of the MgO(001) islands. However, due to the limited resolution present in these spectra it is not possible to discriminate between the majority of F^+ centers located on edges and the minority of centers located on corners that were observed by low-temperature STM/STS investigations.[59]

Because of these limitations we set out to build a machine to improve the spectral resolution. The strategy to achieve this goal is identical to attempts in NMR spectroscopy, namely to increase the operation frequency and in turn the magnetic field. EPR spectroscopy at higher field has developed rapidly in the last two decades, not the least due to the advent of a commercially available instrument (e.g.refs. [60,61]). The present setup builds on the 94 GHz (W-band) spectrometer available from Bruker (ELEXSYS E600). As shown in Figure 4c, this spectrometer was integrated into a multi-chamber ultrahigh vacuum system (for details of the setup please refer to ref. [62]). Apart from ESR spectroscopy, the samples can be characterized using IR spectroscopy, STM, LEED/Auger as well as TPD. At this point we want to focus on the adaptation of the ESR spectrometer.

We resorted to a special resonator design which was used frequently in the early days of high-frequency EPR, namely a Fabry–Perot resonator which will be described in detail elsewhere.[62] We decided to seal the sample in UHV from the rest of the machine by means of a 150 μm thick (diameter 30 mm) quartz window which is located between the mirrors. The Fabry–Perot resonator is built in situ by moving the sample using the long horizontally oriented manipulator (see Figure 4c) into a Ti tube which is situated inside the magnet during the measurements. The sample itself is mounted on a He cryostat and can be cooled to about 60 K. The travelling length of the manipulator is 800 mm. To cope with such a long lever, the entire machine is located on a nonmagnetic optical bench which is placed on active vibration isolation elements. Also, long-term stability of the resonator is needed. To ensure this, we actively manipulate the length of the Ti-tube by means of a Peltier element to compensate for thermal drifts.

Figure 4e shows first measurements under ultrahigh vacuum conditions on a 20 ML thick MgO(001) film grown on Mo(001). The upper spectrum was obtained after adsorption of 4 L (5×10^{-8} torr, 80 s) di-*tert*-butylnitroxide (DTBN). The spectrum consists of a single line with a linewidth of 15 G, which is due to exchange coupling of the molecules and is comparable to findings at the X-band.[63] The lower spectrum was obtained after adsorption of submonolayer coverage (0.5 L) of DTBN. The spectrum shown was obtained after subtraction of a background spectrum acquired after desorption of DTBN at 700 K. The line width of the signal is considerably increased as expected for a system with decreasing exchange interaction. In addition to the exchanged narrowed line, a new signal appears at $g = 1.9985$. This signal is caused by the reaction of DTBN

with the MgO surface. As the number of DTBN molecules present on the surface is known, one can compare the intensity of the exchanged narrowed signal with the one of the new surface species at $g = 1.9985$. This results in a concentration of 1.5×10^{12} spins cm^{-2}, which is currently slightly lower than the sensitivity of the X-band apparatus. However, with this sensitivity and long term stability of the system it is possible to revisit questions related to point defects on oxides which are currently on the way.

6. Conclusions

The advancement of four experimental techniques to investigate nanoscopic systems has been described. The combination of those techniques provides unprecedented information on the relation between geometric structure and properties. This is important as nanoscopic systems, in particular, when interacting with an ambient respond rather differently, more flexibly, compared with a volume system. Such details are actually at the heart of understanding catalysis, a goal we are aspiring to reach. Development of instrumentation is still exceedingly important, and should be forcefully pursued by the scientific community.

Acknowledgements

The work described herein is the result of collaboration of many people who are either mentioned in the text or listed in the references. We are extremely grateful to all of them, in particular to E. Umbach. In addition to the funding from the Max Planck Society, we received support from a number of sources, including the Federal Ministry of Research and Education (BMBF), the German Research Foundation (DFG) through Sonderforschungsbereich SFB 546 and Cluster of Excellence UNICAT, as well as Fonds der Chemischen Industrie.

Keywords: adsorption · catalysis · electron diffraction · electron-spin resonance · surface science

[1] C. B. Duke, *Surf. Sci.* **1994**, *299*/300, vii-viii.
[2] C. B. Duke, E. W. Plummer, *Special Issue of Surface Science Vol. 500: Frontiers in Surface and Interface Science*, North-Holland, Amsterdam, **2002**.
[3] G. Binning, H. Rohrer, *Nobel lecture: Scanning Tunneling Microscopy—From Birth to Adolescence*, **1986**, http://nobelprize.org/nobel prizes/physics/laureates/1986/rohrer-lecture.pdf.
[4] Subcommittee on Nanoscale Science Engineering and Technology, Committee on Technology, National Science and Technology Council, The National Nanotechnology Initiative: Supplement to the President's 2011 Budget, Washington, USA, **2010**.
[5] R. Berndt, J. K. Gimzewski, P. Johansson, *Phys. Rev. Lett.* **1991**, *67*, 3796.
[6] J. H. Coombs, J. K. Gimzewski, B. Reihl, J. K. Sass, R. R. Schlittler, *J. Microsc.* **1988**, *152*, 325–336.
[7] D. Preikszas, Dissertation, Technische Hochschule Darmstadt, **1995**.
[8] D. Preikszas, H. Rose, *J. Electr. Micr.* **1997**, *46*, 1–9.
[9] W. A. Brown, R. Kose, D. A. King, *Chem. Rev.* **1998**, *98*, 797–832.
[10] C. T. Campbell, O. Lytken, *Surf. Sci.* **2009**, *603*, 1365–1372.
[11] J.-H. Fischer-Wolfarth, J. A. Farmer, J. M. Flores-Camacho, A. Genest, I. V. Youdanov, N. Rösch, C. T. Campbell, S. Schauermann, H.-J. Freund, *Phys. Rev. B* **2010**, *81*, 241416.
[12] J.-H. Fischer-Wolfahrt, J. A. Farmer, J. M. Flores-Camacho, C. T. Campbell, S. Schauermann, H.-J. Freund, *unpublished results*.
[13] B. Horn, E. Koch, D. Fick, *Phys. Rev. Lett.* **1984**, *53*, 364.
[14] M. Farle, M. Zomack, K. Baberschke, *Surf. Sci.* **1985**, *160*, 205–216.
[15] R. Berndt in *Springer Series Nanoscience and Technology*, Vol. XII, Springer, Berlin, **1998**, pp. 216.
[16] P. Johansson, R. Monreal, P. Apell, *Phys. Rev. B* **1990**, *42*, 9210.
[17] N. Nilius, A. Cörper, G. Bozdech, N. Ernst, H.-J. Freund, *Prog. Surf. Sci.* **2001**, *67*, 99–121.
[18] G. Hoffmann, J. Kroger, R. Berndt, *Rev. Sci. Instrum.* **2002**, *73*, 305–309.
[19] M. Sakurai, C. Thirstrup, M. Aono, *Phys. Rev. Lett.* **2004**, *93*, 046102.
[20] U. Kreibig, M. Vollmer in *Vol. 25*, Springer, Berlin, **1995**, pp. 1–532.
[21] N. Nilius, N. Ernst, H.-J. Freund, *Phys. Rev. Lett.* **2000**, *84*, 3994–3997.
[22] N. Nilius, H. M. Benia, C. Salzemann, G. Rupprechter, H.-J. Freund, A. Brioude, M. P. Pileni, *Chem. Phys. Lett.* **2005**, *413*, 10–15.
[23] W. Benten, N. Nilius, N. Ernst, H.-J. Freund, *Phys. Rev. B* **2005**, *72*, 045403.
[24] N. Nilius, N. Ernst, H.-J. Freund, *Chem. Phys. Lett.* **2001**, *349*, 351–357.
[25] S. Stankic, M. Müller, O. Diwald, M. Sterrer, E. Knözinger, J. Bernardi, *Angew. Chem.* **2005**, *117*, 4996–4999; *Angew. Chem. Int. Ed.* **2005**, *44*, 4917–4920.
[26] S. Benedetti, H. M. Benia, N. Nilius, S. Valeri, H.-J. Freund, *Chem. Phys. Lett.* **2006**, *430*, 330–335.
[27] a) H. M. Benia, P. Myrach, A. Gonchar, T. Risse, M. Nilius, H.-J. Freund, *Phys. Rev. B* **2010**, *81*, 241415; b) H. M. Benia, P. Myrach, N. Nilius, *New J. Phys.* **2008**, *10*, 013010.
[28] R. Wichtendahl, R. Fink, H. Kuhlenbeck, D. Preikszas, H. Rose, R. Spehr, P. Hartel, W. Engel, R. Schlögl, H.-J. Freund, A. M. Bradshaw, G. Lilienkamp, T. Schmidt, E. Bauer, G. Benner, E. Umbach, *Surf. Rev. Lett.* **1998**, *5*, 1249–1256.
[29] R. Fink, M. R. Weiss, E. Umbach, D. Preikszas, H. Rose, R. Spehr, P. Härtel, W. Engel, R. Degenhardt, R. Wichtendahl, H. Kuhlenbeck, W. Erlebach, K. Ihmann, R. Schlögl, H.-J. Freund, A. M. Bradshaw, G. Lilienkamp, T. Schmidt, E. Bauer, G. Benner, *J. Electron Spectrosc. Relat. Phenom.* **1997**, *84*, 231–250.
[30] T. Schmidt, U. Groh, R. Fink, E. Umbach, O. Schaff, W. Engel, B. Richter, H. Kuhlenbeck, R. Schlögl, H.-J. Freund, A. M. Bradshaw, D. Preikszas, P. Hartel, R. Spehr, H. Rose, G. Lilienkamp, E. D. Bauer, G. Benner, *Surf. Rev. Lett.* **2002**, *9*, 223.
[31] T. Schmidt, S. Heun, J. Slezak, J. Diaz, K. C. Prince, G. Lilienkamp, E. D. Bauer, *Surf. Rev. Lett.* **1998**, *5*, 1287–1296.
[32] H. H. Rotermund, W. Engel, M. Kordesch, G. Ertl, *Nature* **1990**, *343*, 355–357.
[33] E. Bauer, *Rep. Prog. Phys.* **1994**, *57*, 895–938.
[34] J. V. Barth, H. Brune, G. Ertl, R. J. Behm, *Phys. Rev. B* **1990**, *42*, 9307.
[35] D. D. Chambliss, R. J. Wilson, S. Chiang, *J. Vac. Sci. Technol. B* **1991**, *9*, 933–937.
[36] T. Schmidt, H. Marchetto, P. L. Lévesque, U. Groh, F. Maier, D. Preikszas, P. Hartel, R. Spehr, G. Lilienkamp, W. Engel, R. Fink, E. D. Bauer, H. Rose, E. Umbach, H.-J. Freund, *Ultramicroscopy* **2010**, *110*, 1358–1361.
[37] A. Sala, H. Marchetto, T. Schmidt, S. Shaikhutdinov, H.-J. Freund, *unpublished results*.
[38] D. A. King, M. G. Wells, *Surf. Sci.* **1972**, *29*, 454.
[39] H. Conrad, G. Ertl, J. Koch, E. E. Latta, *Surf. Sci.* **1974**, *43*, 462–480.
[40] I. V. Yudanov, R. Sahnoun, K. M. Neyman, N. Rösch, J. Hoffmann, S. Schauermann, V. Johanek, H. Unterhalt, G. Rupprechter, J. Libuda, H.-J. Freund, *J. Phys. Chem. B* **2003**, *107*, 255–264.
[41] S. A. Nepijko, M. Klimenkov, M. Adelt, H. Kuhlenbeck, R. Schlögl, H.-J. Freund, *Langmuir* **1999**, *15*, 5309–5313.
[42] I. V. Yudanov, R. Sahnoun, K. M. Neyman, N. Rösch, *J. Phys. Chem.* **2002**, *117*, 9887–9896.
[43] I. V. Yudanov, M. Metzner, A. Genest, N. Rösch, *J. Phys. Chem. C* **2008**, *112*, 20269–20275.
[44] E. Shustorovich, H. Sellers, *Surf. Sci. Rep.* **1998**, *31*, 1–119.
[45] K. Watanabe, Y. Matsumoto, M. Kampling, K. Al-Shamery, H.-J. Freund, *Angew. Chem.* **1999**, *111*, 2328–2331; *Angew. Chem. Int. Ed.* **1999**, *38*, 2192–2194.
[46] D. Mulugeta, K. H. Kim, K. Watanabe, D. Menzel, H.-J. Freund, *Phys. Rev. Lett.* **2008**, *101*, 146103.
[47] J. H. Lunsford, J. P. Jayne, *J. Phys. Chem.* **1965**, *69*, 2182.
[48] R. D. Iyengar, M. Codell, J. Turkevic, *J. Catal.* **1967**, *9*, 305.

[49] W. L. Hubbell, H. M. McConnell, *J. Am. Chem. Soc.* **1971**, *93*, 314.
[50] M. Yulikov, M. Sterrer, M. Heyde, H. P. Rust, T. Risse, H.-J. Freund, G. Pacchioni, A. Scagnelli, *Phys. Rev. Lett.* **2006**, *96*, 146804.
[51] M. Sterrer, M. Yulikov, E. Fischbach, M. Heyde, H.-P. Rust, G. Pacchioni, T. Risse, H.-J. Freund, *Angew. Chem.* **2006**, *118*, 2692 – 2695; *Angew. Chem. Int. Ed.* **2006**, *45*, 2630 – 2632.
[52] M. Sterrer, E. Fischbach, T. Risse, H.-J. Freund, *Phys. Rev. Lett.* **2005**, *94*, 186101.
[53] J. Schmidt, T. Risse, H. Hamann, H.-J. Freund, *J. Chem. Phys.* **2002**, *116*, 10861 – 10868.
[54] T. Risse, J. Schmidt, H. Hamann, H.-J. Freund, *Angew. Chem.* **2002**, *114*, 1587 – 1591; *Angew. Chem. Int. Ed.* **2002**, *41*, 1517 – 1520.
[55] T. Risse, T. Hill, J. Schmidt, G. Abend, H. Hamann, H.-J. Freund, *J. Phys. Chem. B* **1998**, *102*, 2668 – 2676.
[56] U. J. Katter, T. Hill, T. Risse, H. Schlienz, M. Beckendorf, T. Klüner, H. Hamann, H.-J. Freund, *J. Phys. Chem. B.* **1997**, *101*, 3776 – 3780.
[57] H. Schlienz, M. Beckendorf, U. J. Katter, T. Risse, H.-J. Freund, *Phys. Rev. Lett.* **1995**, *74*, 761 – 764.
[58] M. Zomack, K. Baberschke, *Surf. Sci.* **1986**, *178*, 618 – 624.
[59] M. Sterrer, M. Heyde, M. Novicki, N. Nilius, T. Risse, H. P. Rust, G. Pacchioni, H.-J. Freund, *J. Phys. Chem. B* **2006**, *110*, 46 – 49.
[60] W. Lubitz, K. Mobius, K. P. Dinse, *Magn. Reson. Chem.* **2005**, *43*, S2-S3.
[61] D. Schmalbein, G. G. Maresch, A. Kamlowski, P. Höfer, *Appl. Magn. Reson.* **1999**, *16*, 185 – 205.
[62] E. Kieseritzky, J. Rocker, O. Bondarchuk, A. Seiler, W. Hänsel-Ziegler, T. Risse, H.-J. Freund, *unpublished results*.
[63] U. J. Katter, T. Hill, T. Risse, H. Schlienz, M. Beckendorf, T. Klüner, H. Hamann, H.-J. Freund, *J. Phys. Chem. B* **1997**, *101*, 552 – 560.

Received: September 30, 2010
Published online on November 19, 2010

